



The mechanical behavior of polylactic acid (PLA) films: fabrication, experiments and modelling

S.M. Mirkhalaf^{1,2} · M. Fagerström²

Received: 28 January 2019 / Accepted: 13 September 2019 / Published online: 26 September 2019
© The Author(s) 2019

Abstract Polylactic acid (PLA) is one of the highly applicable bio-polymers in a wide variety of applications including medical fields and packaging. In order to quantitatively model the mechanical behavior of PLA and PLA based bio-composite materials, and also tailor new bio-composites, it is required to characterize the mechanical behavior of PLA. In this study, thin films of PLA are fabricated via hot-pressing, and tensile experiments are performed under different strain rates. To model the mechanical behavior, an elasto-viscoplastic constitutive model, developed in a finite strain setting, is adopted and calibrated. Using the physically-based constitutive model, all regimes of deformation under uniaxial stress state, including post-yield softening, were adequately captured in the simulations. Also, the rate dependency of the stress–strain behavior was properly modelled.

Keywords Polylactic acid (PLA) · Thin films · Mechanical behavior · Elasto-viscoplastic

1 Introduction

PLA is a biodegradable thermoplastic derived from totally renewable resources such as sugar beets and corn. It decomposes to water, carbon dioxide and humus (the black material in soil) (Drumright et al. 2000). Besides, PLA has interesting mechanical properties such as high stiffness and high strength compared to many synthetic polymers (Averett et al. 2011). Physical and mechanical properties of PLA are extensively discussed by Farah et al. (2016). The reader interested in the rheological and thermal properties of PLA and also polymerization process of PLA is referred to Garlotta (2001), Hamad et al. (2015). Also, the already existing manufacturing equipments for petrochemical polymers can be used for PLA as well. Therefore, PLA is proving to be a potential alternative to replace petroleum-derived polymers (Drumright et al. 2000) in different applications such as packaging (Auras et al. 2004;

✉ S.M. Mirkhalaf
mohsen.mirkhalaf@chalmers.se; m.mirkhalaf@gmail.com

¹ Department of Physics, University of Gothenburg, Gothenburg 41296, Sweden

² Division of Material and Computational Mechanics, Department of Industrial and Materials Science, Chalmers University of Technology, Gothenburg, Sweden

Giita Silverajah et al. 2012). Currently, PLA is used in a variety of bio-medical applications as well such as dialysis media and drug delivery devices (Averett et al. 2011). For a review of the potential applications of PLA in different medical fields such as tissue engineering, see Hamad et al. (2015).

Following from rising consciousness about environmental issues and the important need of sustainability, the recent decade has seen considerable developments of bio-composite materials (AL-Oqla and Omari 2017; Mantia and Morreale 2011) to replace composites from synthetic matrices and fibres. In order to use PLA (either neat or in a reinforced state) properly and efficiently, it is necessary to characterize the mechanical properties among other properties. Also, to tailor new bio-composite materials with specific desired properties it is necessary to characterize and model the constituents quantitatively. Rezgui et al. (2005) experimentally investigated the mechanical behavior of PLA injection moulded specimens. The crystalline micro-structure was characterized by WAXS and thermo-mechanical properties by DSC and DMA. Tensile experiments were performed by a video-controlled materials testing system and true stresses and true strains were obtained. Averett et al. (2011) fabricated thin films from neat PLA and PLA reinforced with nanoclay particles and tensile experiments were conducted. Also, fatigue behavior of these materials were experimentally investigated. Qiu et al. (2016) investigated the improvement of PLA ductility by blending with PBS in different weight ratios. Tensile experiments were performed on neat PLA and PLA/PBS blends, and a viscoplastic model (Chaboche 2008) was used to model the rate dependent stress–strain behavior. No strong post-yield softening was observed in the stress–strain curves of PLA/PBS blends.

Not only could PLA be used in a neat form, it could also be considered as an alternative for synthetic polymers for the matrix of composite materials. A strong matrix/fiber interface guarantees a good load transfer between the fibres and matrix and, thereby, ensures that the strong stiffness and strength of fibers are reflected properly in the properties of the composite (Piggott 1987). In order to characterize the interface properties, fibre pull-out test is one of the possible approaches to be followed. To simulate the pull-out test with PLA matrix properly, it is needed to be able to model the PLA matrix quantitatively. However, in spite of relatively considerable amount of experimental studies on the interface characterization and mechanical behavior of PLA based bio-composites, to the authors' knowledge, modelling the interface and mechanical behavior of these materials is not studied extensively.

The goal of this study is to characterize and model the mechanical behavior of PLA as a highly applicable bio-polymer, both neat and as the matrix for bio-composite materials. As it will be shown in the next section, post-yield softening is observed in the mechanical behavior of the PLA under study. The capability to model the post-yield softening (either in neat applications or in a fibre-reinforced state) is important since strain softening causes plastic localization (Govaert et al. 2000). To characterize the mechanical behavior, mechanical experiments are performed on thin films of PLA, fabricated via hot-pressing; and to model the mechanical behavior, an appropriate constitutive model is used. Using the physically based constitutive model, all regimes of the deformation behavior of PLA films under uniaxial tension, including post-yield softening, and also rate dependency of the mechanical behavior were well-captured.

The next section describes how the thin films of PLA are fabricated and the mechanical tests on dog-bone-shaped specimens are conducted. Section 3 describes an elastoviscoplastic constitutive model (Mirkhalaf et al. 2016a) which is used in this study to model the mechanical behavior of PLA. Section 4 gives the experimentally obtained stress–strain curves. Also, details of the material properties determination, simulation results and comparisons to experiments are given in Sect. 4. Finally, Sect. 5 summarizes the concluding remarks of this article and the conclusions drawn from this study.

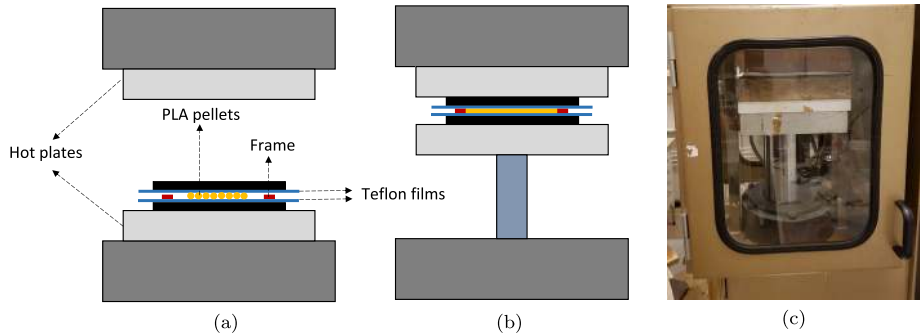


Fig. 1 Schematic representation of two steps of the fabrication process of PLA films with hot-press: (a) first step, (b) second step, and (c) image of the second step

2 Experiments

In this section, the process of fabricating PLA films, as well as the mechanical experiments performed on the films, is explained.

2.1 Fabrication of PLA films

The bio-polymer used in this study is a commercial grade of PLA (Ingeo 3051D) purchased from Nature Works. Thin films are fabricated by hot-pressing from the material, initially in a form of pellets. The temperature of the hot-press plates are set to 190 °C. Teflon films are used to cover the hot-press plates and thin steel films with a thickness of 100 micron are used as a frame. The PLA pellets are kept on the hot plate for 5 minutes to melt. Then, a pressure of 0.5 MPa was applied to the melt for 3 minutes. Once the pressing is over, water cooling is used to return the film back to the ambient temperature. Following the aforementioned process, enough films for the mechanical tests were fabricated. Figure 1 schematically shows two steps of the fabrication process of PLA films via hot-pressing and an image of the pressurized PLA melt.

2.2 Mechanical testing

Dog-bone-shaped specimens were cut from the thin transparent PLA films, and uniaxial tensile experiments were conducted under different loading speeds at room temperature. At the first stage, although no anisotropy was expected (hot-press manufacturing does not normally impose variation of properties in different directions) samples were cut from the films in different loading angles to make sure about the isotropic properties. Figure 2 shows a sample in the tensile machine, a schematic representation of the dog-bone-shaped specimen and a schematic representation of samples cut from the films in different directions. The test machine, shown in Fig. 2a, is a Zwick tensile tester Z2.5, which is equipped with a tensile extensometer.

3 Constitutive model

PLA samples showed the typical behavior of polymeric materials, i.e. initially elastic regime, yield and post-yield softening. Also, the rate dependency of the stress–strain curves

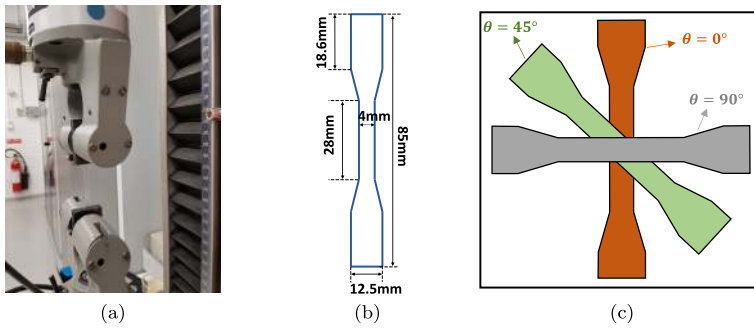
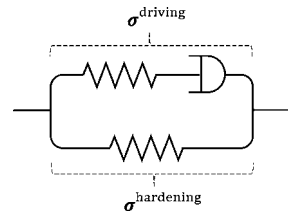


Fig. 2 (a) A dog-bone-shaped sample from a thin PLA film fixed in the tensile machine; (b) schematic representation of the dog-bone-shaped specimen, and (c) schematic representation of samples cut at different angles

Fig. 3 Mechanical analogue of the elasto-viscoplastic model



was clearly seen in the experimental results (see the experimental results in Sect. 4.1). Hence, in this study, an elasto-viscoplastic model, developed by Mirkhalaf et al. (2016a) to predict the mechanical behavior of polymeric materials, is used. The model was developed based on the Eindhoven Glassy Polymer (EGP) model (Govaert et al. 2000) and was used for RVE size determination for heterogeneous polymers (Mirkhalaf et al. 2016b). It was further extended by Mirkhalaf et al. (2017) to predict the behavior of polymeric materials under different loading conditions. This section briefly describes the constitutive model.

Figure 3 shows a schematic representation of the model.

The total stress, τ^{total} , is additively composed of driving stress, $\tau^{driving}$, and hardening stress, $\tau^{hardening}$:

$$\tau^{total} = \tau^{driving} + \tau^{hardening} \tag{1}$$

The driving stress is obtained from the viscous branch of the model and is dependent on the elastic deformation. The driving stress is composed of hydrostatic and deviatoric contributions. On the other hand, the hardening stress depends on the total deformation and is totally deviatoric. In this model, the total deformation gradient, \mathbf{F} , is multiplicatively composed of the elastic deformation gradient, \mathbf{F}^e , and the plastic deformation gradient, \mathbf{F}^p (Bilby et al. 1957):

$$\mathbf{F} = \mathbf{F}^e \mathbf{F}^p \tag{2}$$

The elastic and plastic deformation gradients act on the elastic spring and on the dashpot, respectively. The parallel spring (hardening) is affected by the total deformation gradient. Application of polar decomposition to the elastic and plastic deformation gradients results

in:

$$\mathbf{F}^e = \mathbf{R}^e \mathbf{U}^e = \mathbf{V}^e \mathbf{R}^e, \tag{3}$$

$$\mathbf{F}^p = \mathbf{R}^p \mathbf{U}^p = \mathbf{V}^p \mathbf{R}^p, \tag{4}$$

where \mathbf{R} , \mathbf{U} and \mathbf{V} (for both elastic and plastic deformation gradient tensors) represent the rotation tensor, elastic right stretch tensor and elastic left stretch tensor, respectively. The velocity gradient is defined by

$$\mathbf{L} = \dot{\mathbf{F}}\mathbf{F}^{-1}. \tag{5}$$

Using Eqs. (2) and (5), the velocity gradient can be written as

$$\mathbf{L} = \mathbf{L}^e + \mathbf{F}^e \mathbf{L}^p (\mathbf{F}^e)^{-1}, \tag{6}$$

where \mathbf{L}^e and \mathbf{L}^p denote the elastic and plastic velocity gradients defined by:

$$\mathbf{L}^e \equiv \dot{\mathbf{F}}^e (\mathbf{F}^e)^{-1}, \tag{7}$$

$$\mathbf{L}^p \equiv \dot{\mathbf{F}}^p (\mathbf{F}^p)^{-1}. \tag{8}$$

The plastic stretching tensor (rate of plastic deformation), \mathbf{D}^p , and plastic spin tensor, \mathbf{W}^p , are defined based on the plastic velocity gradient:

$$\mathbf{D}^p \equiv \text{sym}(\mathbf{L}^p) = \frac{1}{2} [\mathbf{L}^p + (\mathbf{L}^p)^T], \tag{9}$$

$$\mathbf{W}^p \equiv \text{skew}(\mathbf{L}^p) = \frac{1}{2} [\mathbf{L}^p - (\mathbf{L}^p)^T], \tag{10}$$

where the superscript T shows the transpose of the tensor. It is assumed that the plastic spin tensor is null ($\mathbf{W}^p = 0$). To measure the elastic deformations, the logarithmic Eulerian strain is adopted, which is given by

$$\boldsymbol{\varepsilon}^e \equiv \ln \mathbf{V}^e = \frac{1}{2} \ln \mathbf{B}^e, \tag{11}$$

where $\ln(\cdot)$ denotes the tensorial logarithm of (\cdot) and \mathbf{B}^e is the left elastic Cauchy–Green deformation tensor defined by

$$\mathbf{B}^e \equiv \mathbf{F}^e [\mathbf{F}^e]^T = [\mathbf{V}^e]^2. \tag{12}$$

The driving Kirchhoff stress is given by

$$\boldsymbol{\tau}^{\text{driving}} = \mathbf{D}^e : \boldsymbol{\varepsilon}^e, \tag{13}$$

where \mathbf{D}^e denotes the fourth order isotropic elastic tensor

$$\mathbf{D}^e \equiv 2G\mathbf{I}_s + \left(K - \frac{2}{3}G \right) (\mathbf{I} \otimes \mathbf{I}), \tag{14}$$

with G and K referring to shear and bulk modulus, respectively. In Eq. (14), the symbol \mathbf{I}_s represents the fourth order symmetric identity tensor and \mathbf{I} is the second order identity tensor. The hardening stress is given by

$$\boldsymbol{\tau}^{\text{hardening}} = H \boldsymbol{\varepsilon}_d, \tag{15}$$

where $\boldsymbol{\epsilon}_d$ denotes the total deviatoric strain and H is the hardening modulus, which is one of the material parameters. The plastic flow rule of the model is given by

$$\mathbf{d}^p = \frac{\mathbf{s}}{2\eta(\tau^{eq})}, \tag{16}$$

where \mathbf{d}^p is the spatial plastic stretching tensor and \mathbf{s} is the deviatoric part of the driving Kirchhoff stress ($\mathbf{s} = \mathbf{l}_d : \boldsymbol{\tau}^{\text{driving}}$), with \mathbf{l}_d being the fourth order deviatoric identity tensor. The spatial plastic stretching tensor, \mathbf{d}^p , is obtained by rotating the plastic stretching tensor, \mathbf{D}^p , to the spatial configuration using the elastic rotation, \mathbf{R}^e , as

$$\mathbf{d}^p \equiv \mathbf{R}^e \mathbf{D}^p \mathbf{R}^{eT}. \tag{17}$$

In Eq. (16), $\eta(\tau^{eq})$ is the viscosity defined by

$$\eta = A_0 \exp\left[\frac{\Delta H}{RT} + \frac{\mu p}{\tau_0} - D_\infty + D_\infty \exp\left(\frac{-h\sqrt{3}\bar{\epsilon}^p}{\sqrt{2}D_\infty}\right)\right] \times \left[\tau^{eq} / \sinh\left(\frac{\tau^{eq}}{\tau_0}\right)\right], \tag{18}$$

where τ^{eq} is the von Mises equivalent stress defined by

$$\tau^{eq} = \sqrt{\frac{1}{2}\mathbf{s} : \mathbf{s}} \tag{19}$$

and $\bar{\epsilon}^p$ is the accumulated plastic strain obtained by temporal integration of the accumulated plastic strain rate defined by

$$\dot{\bar{\epsilon}}^p = \sqrt{\frac{2}{3}\dot{\boldsymbol{\epsilon}}^p : \dot{\boldsymbol{\epsilon}}^p}. \tag{20}$$

In Eq. (18), p is the hydrostatic stress, R is the universal gas constant and T is the absolute temperature. Furthermore, two sets of material properties play a role in the definition of the viscosity function (Eq. (18)): Eyring properties ($A_0, \Delta H, \mu, \tau_0$) and softening properties (h, D_∞). The Eyring (yielding) parameters mainly govern the yielding of the material, and the softening parameters determine how the material softens after yielding.

For a more elaborate discussion on the constitutive model and also the integration algorithm and finite element implementation, the reader is referred to Mirkhalaf et al. (2016a).

4 Results and discussion

In this section, the experimentally obtained stress–strain curves are given, the material properties for PLA under study are determined and simulations are conducted. The model predictions are compared against the experimental results and good agreements are obtained.

4.1 Experimental results

The stress–strain curves at different loading angles under a loading speed of $\dot{u} = 10 \frac{\text{mm}}{\text{min}}$ at room temperature are given in Fig. 4. This loading speed corresponds to an engineering strain rate of $\dot{\epsilon} = 0.006 \text{ s}^{-1}$. As expected, no considerable difference is observed between the stress–strain curves at different loading angles and, as a result, it can be concluded that

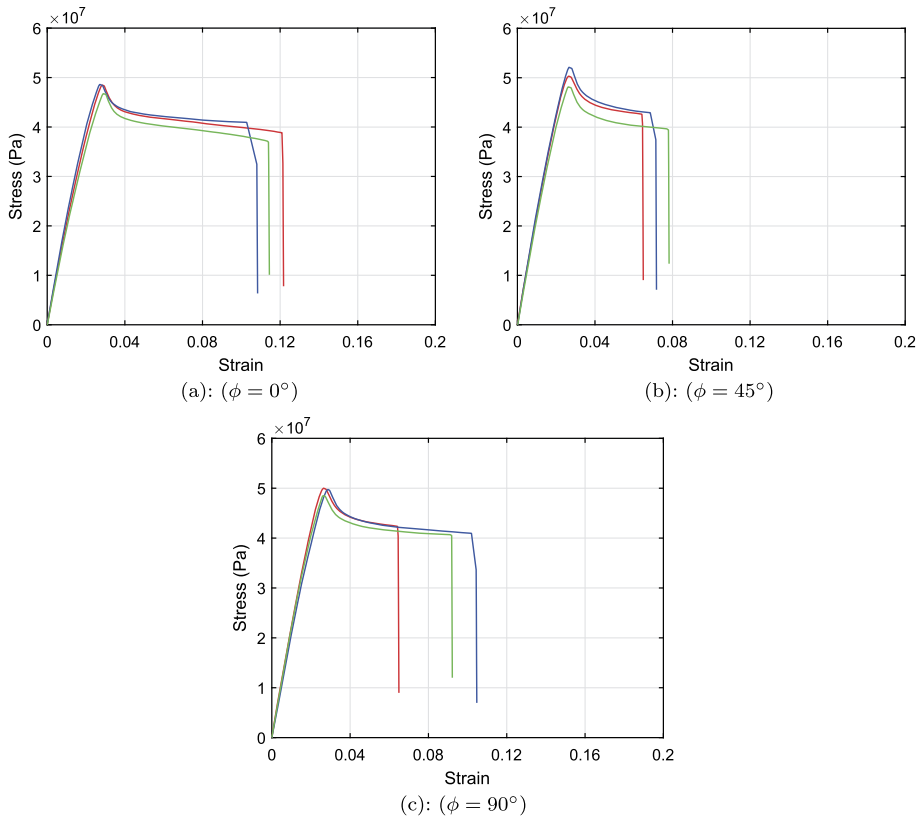


Fig. 4 Experimental stress–strain curves for the samples with different loading angles ($\phi = 0^\circ, 45^\circ, 90^\circ$) under a strain rate of $\dot{\epsilon} = 0.006 \text{ s}^{-1}$ at room temperature (Color figure online)

the films are isotropic. It is remarked that if the samples are manufactured under different processing conditions (such as injection moulding) it is possible to have different mechanical properties in the samples cut at different angles. This is due to the effect of processing condition on the micro-structural formation of polymers (see, e.g. Sedighiamiri 2012).

In order to characterize the rate dependency of the mechanical behavior, tensile experiments are performed at different loading speeds as well (5 and $16.8 \frac{\text{mm}}{\text{min}}$), corresponding to engineering strain rates of $\dot{\epsilon} = 0.003 \text{ s}^{-1}$ and $\dot{\epsilon} = 0.01 \text{ s}^{-1}$, respectively. The stress–strain curves are shown in Fig. 5. Comparing Figs. 4 and 5 show the rate dependency of the mechanical behavior of the PLA films.

4.2 Material properties

To perform the numerical simulations, it is needed to first determine the material properties for PLA required by the constitutive model described in the previous section. The parameters are categorized into four different categories:

- Elastic properties (E, ν);
- Eyring (yielding) properties ($A_0, \Delta H, \tau_0, \mu$);
- Softening properties (h, D_∞);
- Hardening parameter (H).

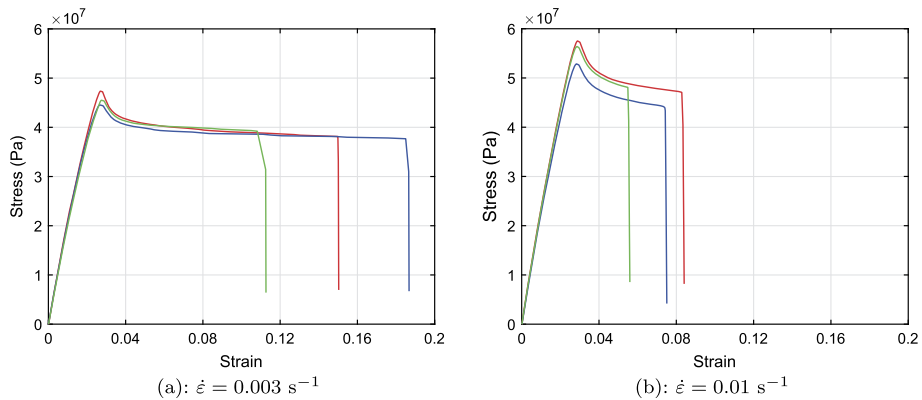


Fig. 5 Experimental stress–strain curves under different strain rates ($\dot{\epsilon} = 0.003 \text{ s}^{-1}$, $\dot{\epsilon} = 0.01 \text{ s}^{-1}$) at room temperature (Color figure online)

Although the difference between the experimental stress–strain curves at each strain rate is negligible, to determine the material properties and compare the simulation results against the experiments, the average of stress–strain curves at each strain rate is considered. The experimental results at two higher strain rates ($\dot{\epsilon} = 0.006$ and 0.01 s^{-1}) are used to quantify the material properties. Then, to confirm that the quantified material properties are applicable to other strain rates too, the properties are used in the simulations for the lowest strain rate ($\dot{\epsilon} = 0.003 \text{ s}^{-1}$).

The Young's modulus is determined according to the slope of the stress–strain curve in the elastic regime ($E = 4400 \text{ MPa}$). Different Poisson's ratios are reported in the literature for PLA samples fabricated via different manufacturing processes (see, e.g. Rezgui et al. 2005; Farah et al. 2016). The Poisson's ratio in this study is assumed as $\nu = 0.3$. It should be mentioned that other values for Poisson's ratio were examined and no considerable change in the results was found. The Eyring (yielding) properties are determined to best capture the yield point at different strain rates. The scalar A_0 is a constant or pre-exponential factor, ΔH is the activation energy, the parameter μ is a pressure coefficient and τ_0 is a characteristic stress. The yield stress prediction increases by increasing the activation energy, the pre-exponential factor and the characteristic stress. On the other hand, increasing the pressure coefficient causes a reduction in the yield stress (Mirkhalaf et al. 2014). Taking into account these effects, a manual fitting procedure was conducted to obtain a set of parameters which gives the best prediction of the experimentally obtained yield stresses. It should be mentioned that the set of Eyring properties may not be unique since they were determined in absence of further calibration. Besides, the determined properties should be carefully used outside the range the strain rates and temperature of this study. The softening properties are calibrated to best predict the post-yield softening regime. One of the softening properties (h) determine the slope of the post-yield regime and the other one (D_∞) governs the saturation value of softening. Finally, the hardening parameter (H) should be quantified which determines how the material hardens once strain softening is over. The determined material properties are tabulated in Table 1.

Remark 1 The mechanical behavior of a polymer sample is dependent on the underlying micro-structure which in turn depends strongly on the thermomechanical history experienced by the sample during processing (Araújo et al. 2014; Hsiung and Cakmak 1993).

Table 1 Material properties for PLA

E (MPa)	ν	ΔH (J/mol)	A_0 (s)	τ_0 (MPa)
4400	0.3	2.062E+5	3.65E−32	5.7
D_∞	h	μ	R	H (MPa)
2.16	450	0.3	8.3143	10

Fig. 6 2D view of spatial discretization of the dog-bone-shaped specimen

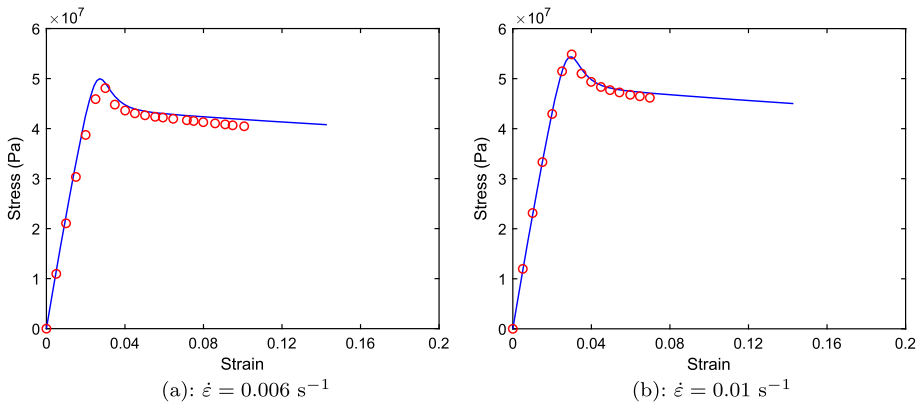
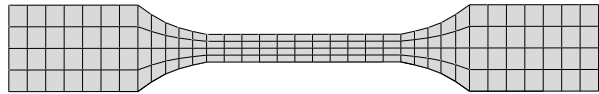


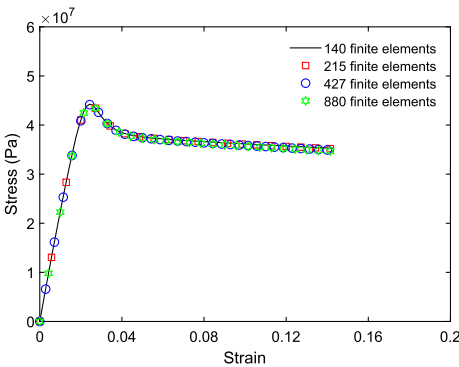
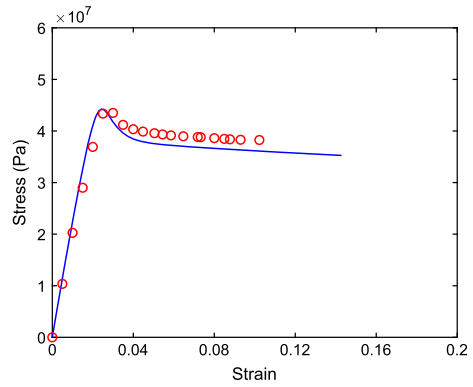
Fig. 7 Comparison between simulations and experimental stress–strain curves under two different strain rates (used to calibrate the material properties); symbols denote experiments and lines illustrate simulations

Thus, polymeric samples manufactured via different fabrication processes typically show different mechanical properties. Hence, the obtained constitutive properties for PLA films in this study (Table 1) should be carefully used for PLA samples fabricated with other manufacturing processes.

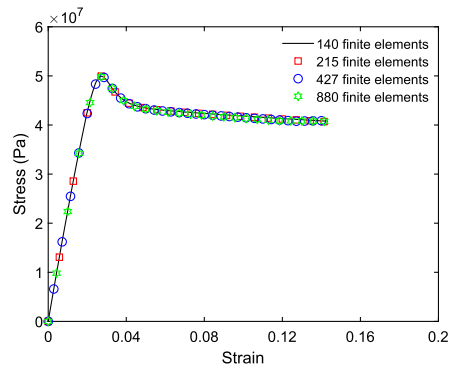
4.3 Simulations and comparison to experiments

The 3D finite element model is shown in a 2D view in Fig. 6 (one element through the thickness). The sample is spatially discretized with 140 three-dimensional eight-noded hexahedron elements. The FE model is used together with the constitutive model, described in Sect. 3, and the determined material properties to conduct the simulations. Figure 7 shows a comparison between the model predictions and the experimental results for the two strain rates ($\dot{\epsilon} = 0.006 \text{ s}^{-1}$ and $\dot{\epsilon} = 0.01 \text{ s}^{-1}$). As mentioned before, the experimental stress–strain curves at two higher strain rates ($\dot{\epsilon} = 0.006 \text{ s}^{-1}$ and $\dot{\epsilon} = 0.01 \text{ s}^{-1}$) are used to determine the material properties. The determined material properties were used for strain rate of $\dot{\epsilon} = 0.003 \text{ s}^{-1}$ for which the comparison between the model predictions and experiments is shown in Fig. 8. It can be seen in Figs. 7 and 8 that good agreements are obtained between the experimental results and simulations.

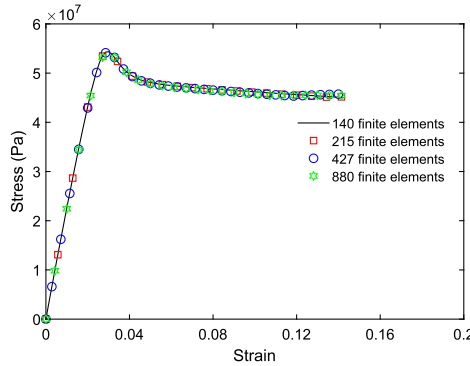
Fig. 8 Experimental stress–strain curve (symbols) against the model prediction (line) for strain rate of $\dot{\epsilon} = 0.003 \text{ s}^{-1}$



(a): $\dot{\epsilon} = 0.003 \text{ s}^{-1}$



(b): $\dot{\epsilon} = 0.006 \text{ s}^{-1}$

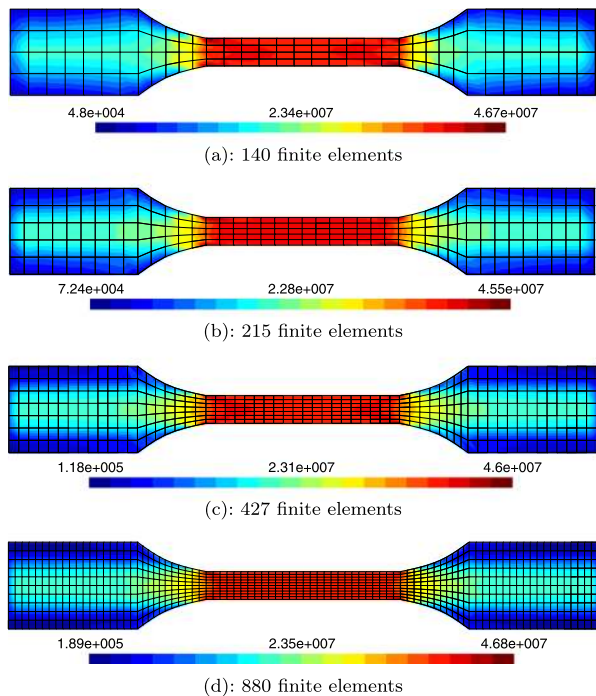


(c): $\dot{\epsilon} = 0.01 \text{ s}^{-1}$

Fig. 9 A comparison between stress–strain curves using four different spatial discretization

Remark 2 It should be emphasized that if a wider range of strain rates was used, it was probably needed to use two viscoplastic flow processes in the constitutive model (see, e.g. Mirkhalaf et al. 2019). This is due to the fact that experimental results on tensile yield behavior of isotropic polymers show that two relaxation processes contribute to the viscoplastic flow (see, e.g. Sedighi-miri et al. 2012). In the range of strain rates used in this study, using one viscoplastic flow process suffices.

Fig. 10 Contour plots of the von Mises effective stress for four different spatial discretizations (Color figure online)



4.4 Assessment of viscoplastic regularization

The constitutive model presented is associated with a viscoplastic regularization technique. The model includes rate effects on the viscoplastic formulation, which implicitly introduces a characteristic length scale through the viscosity function. Therefore, the dependence of the solution on the spatial mesh discretization is attenuated. But, it has been shown in the literature (see, e.g. Niazi et al. 2013 and Dias da Silva 2004) that, although viscous regularization often prevents pathological mesh dependence initially after localization, there is a possibility that the regularization does not last until the end. For certain models, the effective regularization length imposed due to the viscous regularization keeps on decreasing until it approaches the element length. At this moment mesh dependency occurs. Thus, to confirm the objectivity of the obtained results, a mesh dependency analysis is performed. The sample is discretized with three finer FE mesh (215, 427, and 880 finite elements). Simulations are performed at all three strain rates $\dot{\epsilon} = 0.006, 0.003,$ and 0.01 s^{-1} on the FE meshes. Figure 9 shows the stress–strain curves on different FE spatial discretizations at three different strain rates. No considerable dependency on the spatial discretization is observed in the stress–strain curves. Figure 10 shows the contour plots of the von Mises effective stress on the four different spatial discretizations at strain rate of $\dot{\epsilon} = 0.003 \text{ s}^{-1}$. Based on the stress–strain curves, shown in Fig. 9, and the contour plots shown in Fig. 10, it can be concluded that the results obtained using the initial spatial discretization (Fig. 6) are objective.

5 Conclusions

In this study, an experimental investigation of the mechanical behavior of PLA was conducted. PLA films were fabricated from pellets, and dog-bone-shaped specimen were cut for

mechanical testing. Application of different loading speeds on the samples revealed the rate-dependent nature of the material and the necessity of using a viscoplastic model to predict its mechanical behavior. An elasto-viscoplastic model, developed for polymeric materials, was adopted and the material properties were quantified. It was shown that the presented physically-based constitutive model with a set of properly quantified material properties can adequately capture all deformation regimes of PLA (including post-yield softening) under uniaxial tension. Besides, the strain-rate dependent mechanical behavior of PLA was properly captured in the simulations. Furthermore, since the viscous regularization was found to be enough, there was no need for a very fine FE mesh for objective results. This study was an initial step towards developing PLA based bio-composites and predicting their mechanical behavior.

Acknowledgements Open access funding provided by University of Gothenburg. The first and second author acknowledge the financial support from the University of Gothenburg and Area of Advanced Materials Science at Chalmers University of Technology. The second author also acknowledges the support through Vinnova's strategic innovation programme LIGHTer. The authors also thank Robin Nilsson and Massimiliano Mauri for their help in fabrication of PLA films and Dr. Roland Kádár and Abhijit Venkatesh for helping in mechanical testing of films.

Publisher's Note Springer Nature remains neutral with regard to jurisdictional claims in published maps and institutional affiliations.

Open Access This article is distributed under the terms of the Creative Commons Attribution 4.0 International License (<http://creativecommons.org/licenses/by/4.0/>), which permits unrestricted use, distribution, and reproduction in any medium, provided you give appropriate credit to the original author(s) and the source, provide a link to the Creative Commons license, and indicate if changes were made.

References

- AL-Oqla, F.M., Omari, M.A.: Sustainable Biocomposites: Challenges, Potential and Barriers for Development, pp. 13–29. Springer, Cham (2017). https://doi.org/10.1007/978-3-319-46610-1_2
- Araújo, M.C., Martins, J., Mirkhalaf, S., Lanceros-Mendez, S., Pires, F.A., Simoes, R.: Appl. Surf. Sci. **306**, 37 (2014). <https://doi.org/10.1016/j.apsusc.2014.03.072>
- Auras, R., Harte, B., Selke, S.: Macromol. Biosci. **4**(9), 835 (2004). <https://doi.org/10.1002/mabi.200400043>
- Averett, R.D., Realf, M.L., Jacob, K., Cakmak, M., Yalcin, B.: J. Compos. Mater. **45**(26), 2717 (2011). <https://doi.org/10.1177/0021998311410464>
- Bilby, A., Lardner, L., Stroh, A.: In: Actes du IXe congrès international de mécanique appliquée, Bruxelles, vol. 8, p. 35 (1957)
- Chaboche, J.: Int. J. Plast. **24**(10), 1642 (2008). <https://doi.org/10.1016/j.ijplas.2008.03.009>. Special Issue in Honor of Jean-Louis Chaboche
- Dias da Silva, V.: Commun. Numer. Methods Eng. **20**(7), 547 (2004). <https://doi.org/10.1002/cnm.700>
- Drumright, R., Gruber, P., Henton, D.: Adv. Mater. **12**(23), 1841 (2000). [https://doi.org/10.1002/1521-4095\(200012\)12:23<1841::AID-ADMA1841>3.0.CO;2-E](https://doi.org/10.1002/1521-4095(200012)12:23<1841::AID-ADMA1841>3.0.CO;2-E). <https://www.scopus.com/inward/record.uri?eid=2-s2.0-0034505060&doi=10.1002%2f1521-4095%28200012%2912%3a23%3c1841%3a%3aAID-ADMA1841%3e3.0.CO%3b2-E&partnerID=40&md5=d716935c3f015c37ab5915ab5435db3>
- Farah, S., Anderson, D.G., Langer, R.: Adv. Drug Deliv. Rev. **107**, 367 (2016). <https://doi.org/10.1016/j.addr.2016.06.012>. PLA biodegradable polymers
- Garlotta, D.: J. Polym. Environ. **9**(2), 63 (2001). <https://doi.org/10.1023/A:1020200822435>
- Giita Silverajah, V.S., Ibrahim, N.A., Zainuddin, N., Wan Yunus, W.M.Z., Hassan, H.A.: Molecules **17**(10), 11729 (2012). <https://doi.org/10.3390/molecules171011729>
- Govaert, L., Timmermans, P., Brekelmans, W.: J. Eng. Mater. Technol. **122**(2), 177 (2000). <https://doi.org/10.1115/1.482784>. <https://www.scopus.com/inward/record.uri?eid=2-s2.0-0000000527&doi=10.1115%2f1.482784&partnerID=40&md5=4b448d52f54375f07754abfd78f6433>
- Hamad, K., Kaseem, M., Yang, H.W., Deri, F., Ko, Y.G.: eXPRESS Polym. Lett. **9**(5), 435 (2015). <https://doi.org/10.3144/expresspolymlett.2015.42>

- Hsiung, C.M., Cakmak, M.: *J. Appl. Polym. Sci.* **47**(1), 125 (1993). <https://doi.org/10.1002/app.1993.070470116>
- Mantia, F.L., Morreale, M.: *Composites, Part A, Appl. Sci. Manuf.* **42**(6), 579 (2011). <https://doi.org/10.1016/j.compositesa.2011.01.017>
- Mirkhalaf, S., Pires, F., Simões, R.: In: *AES-ATEMA International Conference Series—Advances and Trends in Engineering Materials and their Applications*, vol. 2014, pp. 227–235 (2014). <https://www.scopus.com/inward/record.uri?eid=2-s2.0-84938832362&partnerID=40&md5=91e59b979156ec1253156159fa46a09f>
- Mirkhalaf, S., Andrade Pires, F., Simoes, R.: *Comput. Struct.* **166**, 60 (2016a). <https://doi.org/10.1016/j.compstruc.2016.01.002>. <https://www.scopus.com/inward/record.uri?eid=2-s2.0-84957070657&doi=10.1016%2fj.compstruc.2016.01.002&partnerID=40&md5=2ff0baa9dda57e78ed5156fc90d6692c>
- Mirkhalaf, S., Andrade Pires, F., Simoes, R.: *Finite Elem. Anal. Des.* **119**, 30 (2016b). <https://doi.org/10.1016/j.finel.2016.05.004>. <https://www.scopus.com/inward/record.uri?eid=2-s2.0-84975810854&doi=10.1016%2fj.finel.2016.05.004&partnerID=40&md5=64c17e5a6a4a9391ec1f15b61caa62e2>
- Mirkhalaf, S., Andrade Pires, F., Simoes, R.: *Int. J. Plast.* **88**, 159 (2017). <https://doi.org/10.1016/j.ijplas.2016.10.008>. <https://www.scopus.com/inward/record.uri?eid=2-s2.0-84995811037&doi=10.1016%2fj.ijplas.2016.10.008&partnerID=40&md5=0c1ef28ee863c7420d116740246d1d31>
- Mirkhalaf, M., van Dommelen, J., Govaert, L., Furmanski, J., Geers, M.: *J. Polym. Sci., Part B, Polym. Phys.* **57**(7), 378 (2019). <https://www.scopus.com/inward/record.uri?eid=2-s2.0-85061446380&doi=10.1002%2fpolb.24791&partnerID=40&md5=57d95ad08ccc471aa9afc82a3124f70c>
- Niazi, M.S., Wisselink, H.H., Meinders, T.: *Comput. Mech.* **51**(2), 203 (2013). <https://doi.org/10.1007/s00466-012-0717-7>
- Piggott, M.: *Polym. Compos.* **8**(5), 291 (1987). <https://doi.org/10.1002/pc.750080503>
- Qiu, T.Y., Song, M., Zhao, L.G.: *Mech. Adv. Mat. Mod. Process.* **2**(1), 7 (2016). <https://doi.org/10.1186/s40759-016-0014-9>
- Rezgui, F., Swistek, M., Hiver, J.M., G'Sell, C., Sadoun, T.: *Polymer* **46**(18), 7370 (2005). <https://doi.org/10.1016/j.polymer.2005.03.116>
- Sedighiamiri, A.: *Eindhoven University of Technology* (2012)
- Sedighiamiri, A., Govaert, L., Kanters, M., Van Dommelen, J.: *J. Polym. Sci., Part B, Polym. Phys.* **50**(24), 1664 (2012). <https://www.scopus.com/inward/record.uri?eid=2-s2.0-84869441975&doi=10.1002%2fpolb.23136&partnerID=40&md5=6e6845978879a8f8062dd122a037d7a3>